ARTICLES
https://doi.org/10.1038/s41560-019-0382-6
nature energy

Cation and anion immobilization through chemical bonding enhancement with fluorides for stable halide perovskite solar cells

Nengxu Li[1,11], Shuxia Tao[2,11], Yihua Chen[1], Xiuxiu Niu[3], Chidozie K. Onwudinanti[4], Chen Hu[5], Zhiwen Qiu[1], Ziqi Xu[1], Guanhaojie Zheng[1], Ligang Wang[1], Yu Zhang[1], Liang Li[1], Huifen Liu[1], Yingzhuo Lun[6], Jiawang Hong[6], Xueyun Wang[6], Yuquan Liu[7], Haipeng Xie[7], Yongli Gao[7,8], Yang Bai[3], Shihe Yang[5,9], Geert Brocks[2,10], Qi Chen[3] and Huanping Zhou[1*]

Defects play an important role in the degradation processes of hybrid halide perovskite absorbers, impeding their application for solar cells. Among all defects, halide anion and organic cation vacancies are ubiquitous, promoting ion diffusion and leading to thin-film decomposition at surfaces and grain boundaries. Here, we employ fluoride to simultaneously passivate both anion and cation vacancies, by taking advantage of the extremely high electronegativity of fluoride. We obtain a power conversion efficiency of 21.46% (and a certified 21.3%-efficient cell) in a device based on the caesium, methylammonium (MA) and formamidinium (FA) triple-cation perovskite $(Cs_{0.05}FA_{0.54}MA_{0.41})Pb(I_{0.98}Br_{0.02})_3$ treated with sodium fluoride. The device retains 90% of its original power conversion efficiency after 1,000 h of operation at the maximum power point. With the help of first-principles density functional theory calculations, we argue that the fluoride ions suppress the formation of halide anion and organic cation vacancies, through a unique strengthening of the chemical bonds with the surrounding lead and organic cations.

Organic–inorganic halide perovskites (ABX_3, where A is an organic cation, such as methylamine (MA) or formamidine (FA); B is lead or tin; X is a halide ion) have emerged as exciting new materials for solar cells due to their unique combination of properties, such as strong light absorption[1], superb charge carrier mobility[2] and low-cost fabrication[3]. Power conversion efficiencies (PCEs) of perovskite solar cells (PSCs) have risen from 3.8% to a certified 23.7%[1,4–10], close to that of crystalline silicon solar cells. In spite of the unparalleled growth in photovoltaic performance, the industrial application of PSCs is hampered by instability issues. One of the main sources of the instability is the defect chemistry of perovskites. In particular, owing to the ionic nature of perovskite materials[11], as well as their solution-based fabrication processes, numerous defects are formed at the surfaces and grain boundaries of polycrystalline perovskite films[12–15]. In particular, point defects such as halide anion vacancies and organic cation vacancies are easily produced in perovskite materials due to their low formation energies[16–18]. Although these defects mostly create shallow electronic levels near the band edges[8,19], they still have profound unwanted effects on carrier dynamics and the *I–V* hysteresis of PSCs[20–23]. Even more importantly, such defects are believed to play an important role in the chemical degradation of the perovskite material and of the interfaces with the charge transport layers, leading to long-term instability of the PSCs[24–27]. Ion vacancies diffuse into the crystallites, and promote the diffusion of cations and anions to the surfaces and grain boundaries. Decomposition reactions at these locations, such as evaporation of the organic species MA or FA, then lead to degradation of the material. Therefore, control and mitigation of the number of organic cation or halide anion vacancies has become an important research direction towards more efficient and stable PSCs.

As organic components such as MA or FA easily evaporate from the surface during the thermal annealing process[11,28], thereby creating organic cation vacancies, one way to suppress the formation of such vacancies is to use excess MA/FA during or after the perovskite annealing process[29]. Another approach to prevent the formation of organic cation vacancies is to create a two-dimensional layered structure by introducing a small amount of larger organic molecules, such as phenethylamine, polyethylenimine and trifluoroethylamine, which are difficult to evaporate[30]. Similar methods have also been reported to be effective for passivating or suppressing halide anion vacancies[8,31,32]. Previously, iodide ions have been introduced into the organic cation solution, which decreases the concentration of iodide vacancies[8]. Elsewhere, guanidinium, an organic ion that probably forms hydrogen bonds, has been used to suppress the formation of iodide vacancies[31]. Addition of KI to perovskites has also demonstrated a positive effect of small alkali ions on

[1]Beijing Key Laboratory for Theory and Technology of Advanced Battery Materials, Key Laboratory of Polymer Chemistry and Physics of Ministry of Education, Department of Materials Science and Engineering, College of Engineering, Peking University, Beijing, China. [2]Center for Computational Energy Research, Applied Physics, Eindhoven University of Technology, Eindhoven, the Netherlands. [3]Experimental Center for Advanced Materials, School of Materials Science and Engineering, Beijing Institute of Technology, Beijing, China. [4]Center for Computational Energy Research, DIFFER—Dutch Institute for Fundamental Energy Research, Eindhoven, the Netherlands. [5]Department of Chemistry, The Hong Kong University of Science and Technology, Hong Kong, China. [6]School of Aerospace Engineering, Beijing Institute of Technology, Beijing, China. [7]Hunan Key Laboratory for Super-Microstructure and Ultrafast Process, College of Physics and Electronics, Central South University, Changsha, China. [8]Department of Physics and Astronomy, University of Rochester, Rochester, NY, USA. [9]Guangdong Key Lab of Nano-Micro Material Research, School of Chemical Biology and Biotechnology, Shenzhen Graduate School, Peking University, Shenzhen, China. [10]Computational Materials Science, Faculty of Science and Technology and MESA+ Institute for Nanotechnology, University of Twente, Enschede, the Netherlands. [11]These authors contributed equally: Nengxu Li, Shuxia Tao. *e-mail: happy_zhou@pku.edu.cn

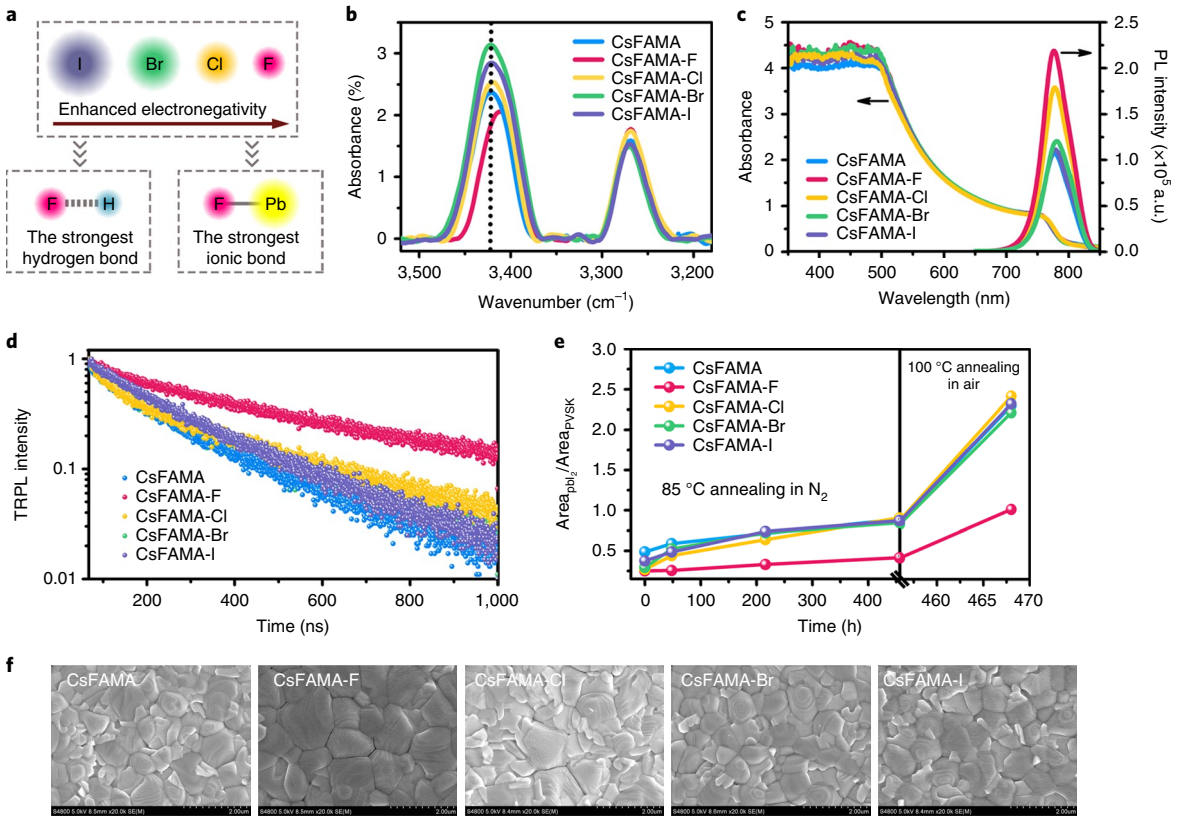

Fig. 1 | The characterization of perovskite thin films (CsFAMA and CsFAMA-X). a, A schematic illustration of enhancing the hydrogen bond between the halogen and MA/FA ions, and strengthening the ionic bond between the halogen and metal ions through increasing the electronegativity of halogen. **b**, Reflectance micro-Fourier transform infrared spectroscopy. The black dotted line indicates the N-H vibrations of the MA/FA ions. **c**, Ultraviolet-visible absorption spectra and steady-state PL spectra. **d**, TRPL spectra with a log scale for the *y* axis. **e**, The evolution of the relative content of the PbI_2 phase in the perovskite film, expressed as the ratio of the X-ray diffraction peak areas for the PbI_2 and the perovskite signals; the results are for films maintained at 85 °C in nitrogen (456 h) and subsequently annealed at 100 °C (12 h) in air. **f**, Top-view FE-SEM images of perovskite films. Scale bars, 2 μm.

passivating I^- vacancies, which consequently improves the efficiency and stability of PSCs[33–35]. In addition, small ions (Cl and Cd) were doped into the perovskite lattice to suppress the formation of halide vacancies via lattice strain relaxation[26]. Although significant advances have been made in defect engineering of the bulk and grain boundaries of perovskites, most strategies focus on passivating or preventing only one type of defect, either the organic cation or the halide anion vacancy. Only recently, choline chloride was used to passivate both positive and negative charged defects by quaternary ammonium and halide ions[11]. This 'charged components compensation' provides a possible method of multi-vacancy defects passivation.

Here we report a chemical bonding modulation of perovskite films by tuning the bond strength of the additives with the perovskites. We start from the state-of-the-art triple-cation perovskite $(Cs_{0.05}FA_{0.54}MA_{0.41})Pb(I_{0.98}Br_{0.02})_3$ absorber and add a small amount of alkali halide, NaX (X = I, Br, Cl or F), using a two-step solution process (for details, see Methods). Although all alkali halides improve the quality of the perovskite, the fluoride-containing material gives by far the best performance. Planar n–i–p solar cells made on the basis of the fluoride-containing perovskite yield a PCE of 21.46% (and a certified 21.3%-efficient solar cell). More importantly, non-encapsulated PSCs using the fluoride-containing materials exhibit an excellent long-term stability. They retain 90% of their original PCE after 1,000 h of continuous illumination under maximum power point (MPP) operating conditions, or under thermal stress of 85 °C. From results obtained with a wide range of experimental characterization techniques and density functional theory (DFT) calculations, we argue that the fluoride ions are very effective in passivating both the organic cation and halide anion vacancies by forming strong hydrogen bonds (N–H···F) with organic cations (MA/FA) and strong ionic bonds with lead in the perovskite films.

Properties of CsFAMA-X films

Passing through the halide series I, Br, Cl and F (Fig. 1a), the electronegativity increases and the ionic radius becomes smaller. This leads to an increased chemical bonding between the halide anions with the A and B cations. In the following, we first compare the properties of the $(Cs_{0.05}FA_{0.54}MA_{0.41})Pb(I_{0.98}Br_{0.02})_3$ perovskite, modified by adding 0.1% NaX (X = I, Br, Cl, or F), to those of the unmodified perovskite as a reference. We denote the reference perovskite as 'CsFAMA' and the NaX-containing perovskite as 'CsFAMA-X'.

Figure 1b shows the reflectance micro-Fourier transform infrared spectra of CsFAMA and CsFAMA-X films. Compared to the reference CsFAMA, the spectrum of the CsFAMA-F film shows a substantial shift of the N–H vibration modes (3,500–3,350 cm^{-1}) towards a lower wavenumber. This kind of shift is absent in the CsFAMA-X (X = I, Br, Cl) samples. We attribute this shift to the formation of hydrogen bonds N–H···F between the FA/MA and F species[36]. This hydrogen bond results in a delocalization of the electronic cloud of the N–H bond. It weakens the N–H chemical bond, which decreases the corresponding vibrational frequency. Our solid-state ^1H NMR measurements also confirm the formation of hydrogen bonds between the fluoride and the MA ions, as evidenced by the larger chemical shift of NH_3 protons in the CsFAMA-F sample (Supplementary Fig. 1).

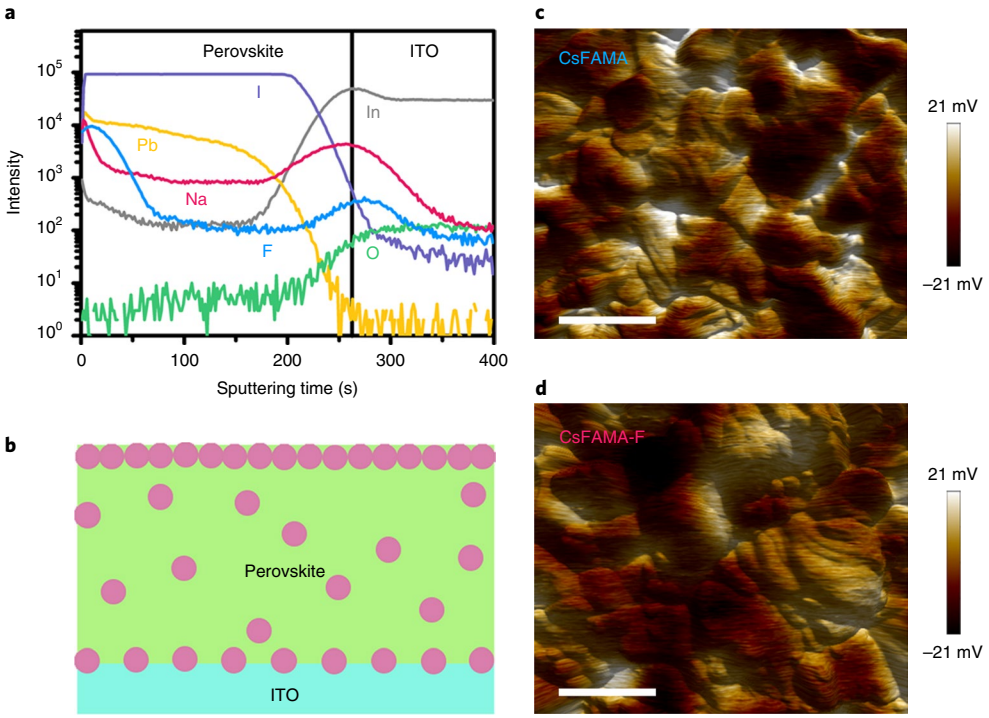

Fig. 2 | Surface and bulk characterization of perovskite films. a, ToF-SIMS depth profile analysis of a CsFAMA-F perovskite sample. **b**, A scheme of the possible location of NaF (pink circles) across the perovskite films. **c**,**d**, Scanning Kelvin probe microscopy measurements: combining topography spatial maps and surface potential values of CsFAMA (**c**) and CsFAMA-F (**d**) perovskites. Scale bars, 1 μm. The colour scale bar from black to white represents the surface potential varied from -21 mV to 21 mV in **c** and **d**.

These experimental findings are supported by DFT calculations (Supplementary Fig. 2). Our calculations show that the presence of a fluoride ion at the surface induces the reorientation of several adjacent FA cations, and the formation of N–H···F hydrogen bonds. As a result, the stretching modes of the corresponding N–H groups shift to lower frequencies. Averaged over the stretching modes of all N–H groups of the affected FA ions, this leads to an overall shift of 63 cm^{-1}. DFT results also indicate that the inclusion of a sodium ion has negligible effects on these vibration modes, confirming that fluoride is responsible for the change in the vibration dynamics of the FA cations. As we will discuss later, the strong fluoride–organic cation interaction significantly stabilizes the perovskite surface and suppresses the formation of organic cation vacancies.

The effects of NaX additives on the optical properties and the structure of the perovskite thin films are carefully investigated by a range of techniques. The bandgap of the CsFAMA-X films is the same as that of the reference CsFAMA, according to ultraviolet–visible and photoluminescence (PL) spectra (Fig. 1c). Neither shifts in the peaks, nor new peaks are observed in the X-ray diffraction patterns (Supplementary Fig. 3), indicating that addition of NaX does not alter the crystal structure of the perovskite films. Whereas these basic optical and crystal structural properties of all CsFAMA-X films are similar, time-resolved PL (TRPL) results (Fig. 1d and Supplementary Table 1) reveal an important difference in the lifetime of free charge carriers between the CsFAMA and the CsFAMA-X films. The CsFAMA-F sample exhibits carrier lifetimes (τ_1: 97.16 ns, τ_2: 401.64 ns) that are much longer than those of the CsFAMA reference (τ_1: 30.82 ns, τ_2: 193.29 ns). In contrast, the carrier lifetimes of the other CsFAMA-X (X = I, Br, Cl) samples are much closer to those of the reference. This implies that non-radiative recombination is effectively suppressed by the addition of fluoride.

It should be noted here that another difference between the CsFAMA-X films can be found from field-emission scanning electron microscopy (FE-SEM) images (Fig. 1f). We observe that CsFAMA-Cl and CsFAMA-F films exhibit a slightly larger grain size than that of CsFAMA-Br and CsFAMA-I, which is probably due to the fact that the chloride and fluoride may influence the crystal nucleation and crystallization kinetics of perovskites (Supplementary Figs. 4 and 5). As shown from the TRPL results above and thermal stability properties in the following paragraph, the effect of the NaF additive is much more pronounced than that of NaCl, implying that the larger grain size, while a contributing factor, does not explain all of the improvements found in CsFAMA-F films.

We explore the thermal stability of the perovskite films by maintaining them at 85 °C in a nitrogen atmosphere, followed by a thermal annealing at 100 °C in air. During these ageing tests, we monitor the relative content of PbI_2 via X-ray diffraction patterns (Supplementary Fig. 3), given that PbI_2 is one of the known decomposition products of perovskites. Figure 1e summarizes the relative X-ray diffraction intensity of PbI_2 and perovskite in the films. Clearly the CsFAMA-F film has a much lower PbI_2 content than all of the other films, which confirms the outstanding thermal stability of this material. The main degradation reactions caused by thermal stress are the deprotonation and desorption of volatile organic cations[37]. The improvement in thermal stability observed in the CsFAMA-F sample is attributed to the hydrogen bonds between the fluoride and MA/FA ions inhibiting the diffusion and dissociation of organic cations.

In short, of the halide salts studied, NaF enables the greatest improvements in terms of thermal stability and carrier lifetimes in CsFAMA perovskites. Therefore, in the following, we focus on CsFAMA-F and the role played by the fluoride in the context of photovoltaics performance of solar cells made with this material.

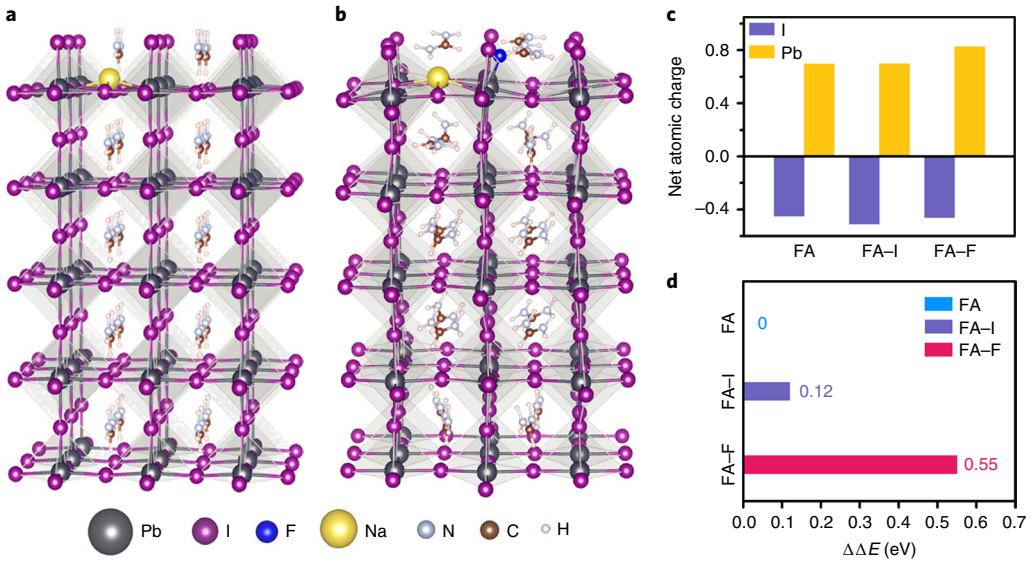

Fig. 3 | Location of Na and F ions and effects on chemical bonding strength and formation energy of FA vacancies. a,**b**, Optimized structures of a Na–I unit (**a**) and a Na–F unit (**b**) adjacent to the $FAPbI_3$ surface. The yellow, blue, purple, black, grey, brown and orange spheres denote the Na, F, I, Pb, N, C and H ions, respectively. **c**, Net atomic charges of I and Pb ions on the $FAPbI_3$ surface with incorporation of NaI species (FA-I) or NaF species (FA-F), and without any incorporation (FA). **d**, Formation energy of a surface FA vacancy in the clean $FAPbI_3$ (FA), and in the NaI (FA-I) or NaF (FA-F) species incorporated surfaces.

Possible location of fluoride and its passivation effects

To investigate the presence and distribution of NaF in the perovskite film, time-of-flight secondary-ion mass spectroscopy (ToF-SIMS) is employed to probe the depth profiles of the atomic species in the CsFAMA-F perovskite sample (Fig. 2a). The maximum signals of Na and F are observed on the surface of the perovskite thin film and at the perovskite/ITO interface. Nevertheless, signals with appreciable intensity are observed along the entire film thickness. The presence of NaF in the film is also confirmed by the energy-dispersive X-ray spectroscopy results, as shown in Supplementary Fig. 6. As no significant peak shifts are observed in X-ray diffraction results, it rules out the possibility of NaF entering the CsFAMA crystal lattice (Supplementary Fig. 3). As analysed above, we therefore suggest that NaF is indeed in the film, possibly concentrated at the surface, as illustrated by Fig. 2b.

To probe the effect of NaF at the surface of the perovskite film, we apply scanning Kelvin probe microscopy[38,39], and combine a three-dimensional spatial map of the topography and a map of the surface potential. In the reference sample (CsFAMA), the surface potential at the boundaries of the grains is 40 mV higher than in the middle of the grains (see Fig. 2c). In the CsFAMA-F sample (Fig. 2d), this surface potential difference is only about 20 mV. We conclude that NaF modifies the surface potential (Supplementary Fig. 7), which further suggests that NaF species are probably located at the surface.

To gather more atomistic information regarding the possible location of NaF and its effect on the stability of the perovskite, we calculate the relative energies of incorporation of Na and F ions in the bulk and on surfaces, using DFT. The Na ion is found to be more stable on surfaces than in the bulk by 0.2 to 0.3 eV. On both FAI- and PbI_2-terminated surfaces, Na preferentially occupies an interstitial site, rather than an A site (Supplementary Fig. 8). A detailed chemical analysis (Fig. 3c) shows that incorporation of a Na ion increases the ionic charge on the nearby I ions. It indicates that Na may play a role in suppressing the diffusion of halide ions.

We find that incorporating a F ion into the perovskite lattice is extremely difficult, and it has a strong preference for staying at the surface. By far the most energetically favourable position of a F ion is substitution of an I ion at an FAI-terminated surface. Positions of F ions either in the perovskite bulk, or in a PbI_2-terminated surface, have an energy that is about 3.5 eV higher (Supplementary Fig. 9). The size mismatch between I and F ions probably prevents the latter from being incorporated comfortably inside the perovskite lattice, as it would induce too much strain. This is avoided by incorporating F ions on the FAI surface.

However, the incorporation of F ions on the FAI surface changes the local bonding at the surface and subsurface layers. The most dramatic change is that the FA cations surrounding a F site reorient towards the F ion, in such a way as to maximize their interactions with this ion (Fig. 3a,b). This is in agreement with the N–H vibration mode analysis discussed above (Fig. 1b and Supplementary Fig. 2), supporting the finding that FA ions closest to a F site form hydrogen bonds with the F ion. In addition, the ionic charge on the Pb ions surrounding a F site also increases (Fig. 3c), indicating that the F ions form stronger ionic bonds. In summary, the introduction of F at FAI-terminated surfaces stabilizes the local structure via increased bonding with Pb, and via hydrogen bonds with FA ions.

To further elucidate the effect of incorporation of F ions, we calculate the formation energies of FA cation vacancies on the surface of the clean perovskite, and that on the surfaces incorporated with NaI or NaF species (Fig. 3d and Supplementary Fig. 10). Whereas the FA vacancy formation energy close to a NaI species increases by a mere 0.12 eV, compared to the pristine perovskite, close to a F ion it increases by a sizeable 0.55 eV. The presence of F therefore significantly prevents the formation of FA vacancies at the surface. This result supports the excellent thermal stability of the CsFAMA-X perovskite films (Fig. 1e), where the creation of organic cation vacancies is typically believed to be responsible for the degradation of the perovskites under thermal stress.

Solar cell performance

To investigate the photovoltaics performance based on our improved material, we fabricate n–i–p planar PSCs using CsFAMA and CsFAMA-F perovskites as the absorbers. The cross-sectional SEM image in Fig. 4a shows the device structure, which comprises

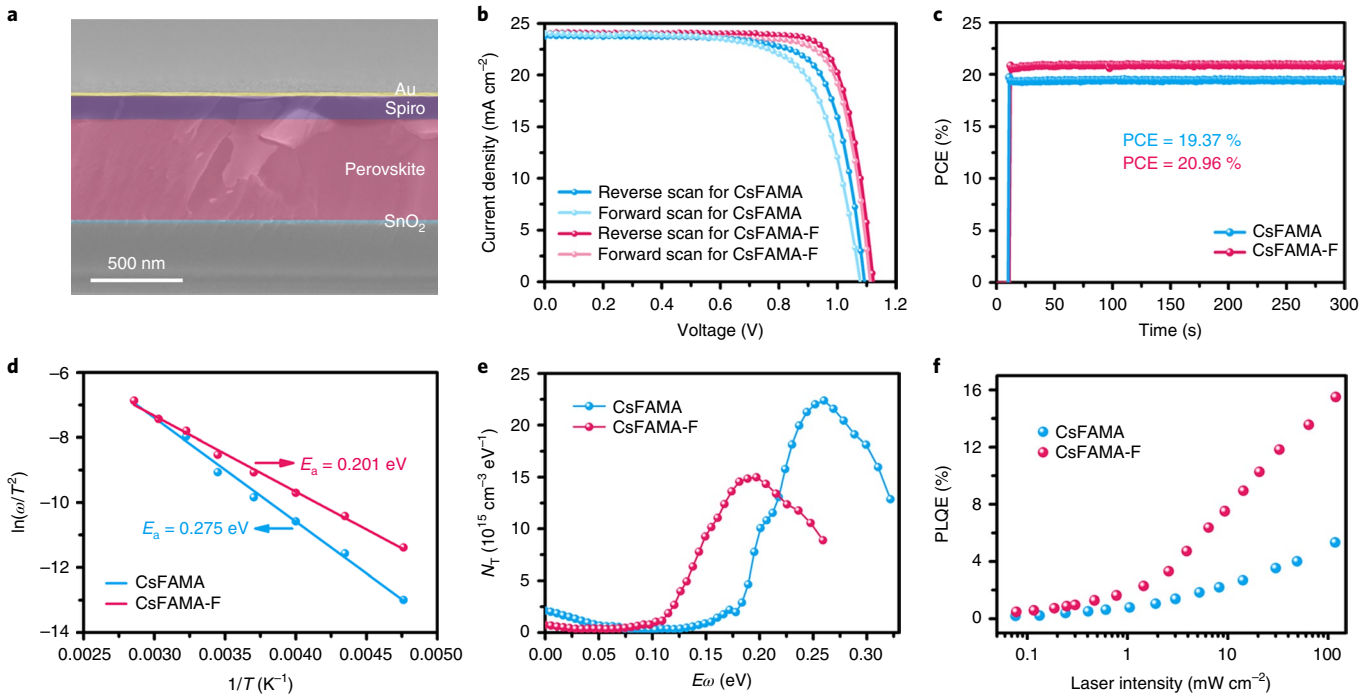

Fig. 4 | Performance of PSCs. a, A cross-sectional SEM image. **b**, *J*–*V* curves with reverse (1.2 V to −0.2 V) and forward (−0.2 V to 1.2 V) scans of devices made with the untreated material (CsFAMA) and with the NaF-treated perovskite (CsFAMA-F). The scan rate is 100 mV s^{-1}. **c**, Stabilized PCEs at the MPP (voltage 0.92 V for the CsFAMA sample, 0.94 V for the CsFAMA-F sample). **d**, Arrhenius plots (obtained by linear fitting of data points) of the characteristic transition frequencies determined from the derivative of the admittance spectra. **e**, Trap state density (N_T) of the perovskite solar devices measured at 290 K. **f**, PLQE of perovskite films as a function of excitation power.

an ITO glass substrate covered by a 50-nm-thick SnO_2 electron transport layer. On top of that we deposit a 600-nm-thick perovskite film, covered with a layer of Spiro-OMeTAD as the hole transport layer (200 nm), and an 80-nm-thick gold electrode as the back contact.

As summarized in Table 1 and shown in Fig. 4b, the CsFAMA-F cells give rise to a PCE of 21.46% (average value from reverse and forward scan results) with negligible *J*–*V* hysteresis. This is to be compared to the reference CsFAMA with an average PCE of 19.03% with moderate *J*–*V* hysteresis. Examples of CsFAMA and CaFAMA-X cells with stabilized PCEs of 19.37% and 20.96%, respectively, are shown in Fig. 4c. The statistics of 60 devices with or without NaF are shown in Supplementary Fig. 11 and Supplementary Table 2. The average PCEs for the CsFAMA and CaFAMA-F devices are 18.86% and 20.56%, respectively. The short-circuit current density (J_{sc}) increases only slightly in CsFAMA-F cells (the spectral responses of the external quantum efficiency of these devices are shown in Supplementary Fig. 13), while the most dramatic enhancement is found in the open-circuit voltage (V_{oc}) and fill factor (FF). We attribute this improvement to the immobilization of mobile ions and vacancy defects such as iodide and MA (FA) due to the incorporation of fluoride ions. The best CsFAMA-F device has been certified by a third party (Supplementary Fig. 12). The certified PCEs are 21.7% under the reverse scan direction (1.2 to −0.1 V) and 20.8% under the forward scan direction (−0.1 to 1.2 V), with a slow scan rate (33 mV s^{-1}) under AM1.5G full-sun illumination (1,000 W m^{-2}). This certified efficiency of 21.3% (average value from certified reverse and forward scan results) agrees well with measured performances in our own laboratory.

To examine the effects of incorporation of NaF on the defects in the perovskite absorber, we use admittance spectroscopy, and conduct a Mott–Schottky analysis to analyse the defects profile. We first conduct temperature-dependent admittance spectroscopy measurements on the CsFAMA and CsFAMA-F devices with the temperature rising from 210 to 350 K without illumination (Supplementary Fig. 14a,b). Subsequently, the defect activation energies (E_a) in the CsFAMA and CsFAMA-F samples are calculated to be 0.275 and 0.201 eV, respectively (Fig. 4d). The trap density-of-states distribution and their energy levels are presented in Fig. 4e. Incorporation of fluoride effectively reduces the energy level of trap states from 0.26 to 0.18 eV, as well as their density of states from 22.4×10^{15} to 14.9×10^{15} cm^{-3} eV^{-1}.

We have further carried out PL quantum efficiency (PLQE) measurements. Figure 4f shows that the CsFAMA-F sample has a higher PLQE compared to the CsFAMA sample. Moreover, its PLQE increases more rapidly with increasing laser intensity. Space-charge-limited current measurements, transient photovoltage, transient photocurrent decay experiments and ultraviolet photoelectron spectroscopy (UPS) measurements all show agreement with our finding that NaF effectively passivates electronic defects in PSCs, which is responsible for the improved PCE (see Supplementary Notes 11–13 and Supplementary Figs. 15–17).

Table 1 | Photovoltaics parameters for the best CsFAMA solar cell and the best CsFAMA-F cell under the forward (−0.2 to 1.2 V) and reverse (1.2 to −0.2 V) scan directions

Sample	V_{oc} (V)	J_{sc} (mA cm^{-2})	FF (%)	PCE (%)
CsFAMA, forward	1.079	23.72	71.79	18.38
CsFAMA, reverse	1.095	24.03	74.77	19.68
CsFAMA-F, forward	1.112	24.01	78.62	20.99
CsFAMA-F, reverse	1.126	24.23	80.35	21.92

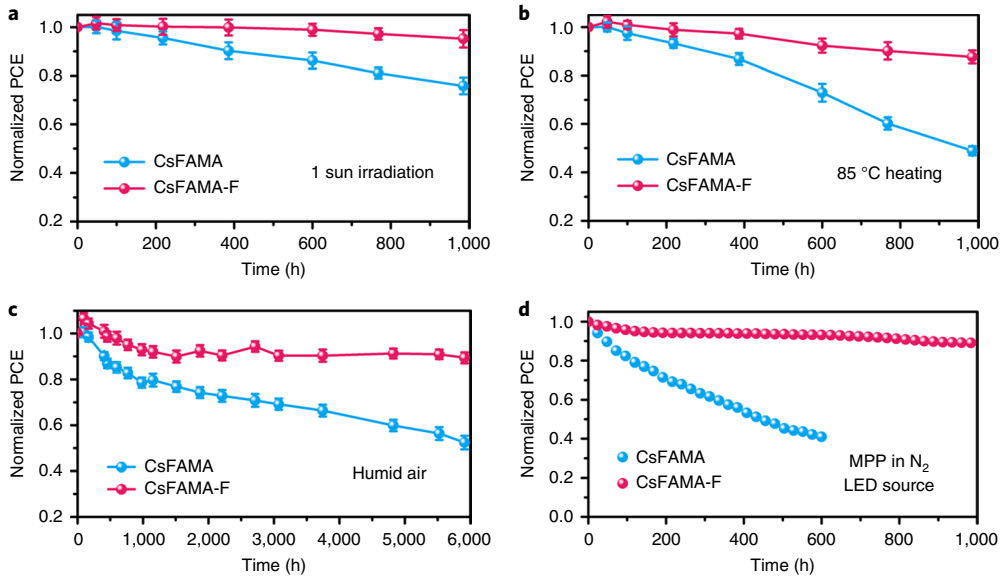

Fig. 5 | Stability performance of PSCs under various conditions. All devices are unencapsulated and CsFAMA devices are compared with NaF-containing devices. **a**, Evolution of normalized PCEs of devices on continuous one-sun illumination in a nitrogen atmosphere. **b**, Devices kept at 85 °C in a nitrogen atmosphere. In **a** and **b**, the error bars represent the standard deviation for six devices. **c**, Devices in ambient air with a relative humidity of about 25%–45%, and a temperature of about 25–40 °C. The error bars represent the standard deviation for eight devices. **d**, Devices under MPP tracking and continuous light irradiation with a white LED lamp, 100 mW cm^{-2} in a nitrogen atmosphere. Note that the initial efficiencies of these PSCs are about 19% for CsFAMA, and 20% for CsFAMA-F.

To establish the stability of our improved CsFAMA-F material, we carry out a series of investigations on unencapsulated devices. The results of stability tests under continuous one-sun illumination, or at a fixed temperature of 85 °C in a nitrogen atmosphere, are shown in Fig. 5a,b. The photo-stability of CsFAMA-F-based cells is superior to that of the reference cells, maintaining 95% of their original PCE after 1,000 h of illumination. As shown in Fig. 5b, the thermal stability of F-containing devices shows an even more significant improvement. The CsFAMA-F-based devices retain 90% of their initial PCE after annealing at 85 °C for 1,000 h, while CsFAMA PSCs retain only 50% of their initial PCE. We attribute this to the excellent thermal stability of NaF-containing perovskite films (Fig. 1e).

In addition, we probe the storage lifetime of devices in an environment with humidity of about 25%–45% at a temperature of about 25–40 °C (Fig. 5c). The evolution of the normalized PCE shows that CsFAMA-F cells exhibit a significantly improved long-term stability, retaining 90% of their original PCE after over 6,000 h of storage in ambient air.

Most importantly, we investigate the operational stability of unencapsulated devices under MPP tracking with a continuous one-sun irradiation in a nitrogen atmosphere (Fig. 5d). The reference cells show a rapid loss of PCE (below 40% of the original PCE after working for 600 h), while the CsFAMA-F cell exhibits a long lifetime, retaining over 90% of its initial PCE after 1,000 h. In addition, we also investigate the operational stability of unencapsulated PSCs under MPP tracking with continuous light irradiation (solar simulator source, 100 mW cm^{-2}) in air (Supplementary Fig. 18). It can be found that CsFAMA-F PSCs exhibit superior stability performance compared with reference cells (CsFAMA): the CsFAMA-F cells retain 85% of their PCE after 350 min, while the PCE of the CsFAMA reference cells drops below 60% in less than 50 min, which further confirms that the incorporation of NaF in the perovskite film brought about remarkable improvements in the long-term stability of PSCs.

It is important to emphasize that the effect of NaF is different from that of other sodium halides NaX (X = Cl, Br, I). To demonstrate this, we fabricate PSCs based on CsFAMA absorbers treated with other sodium halides. The corresponding PCEs are then slightly improved compared to the untreated CsFAMA (Supplementary Fig. 19a), which is in line with other reports[40]. However, these devices exhibit an obvious *J*–*V* hysteresis (larger hysteresis index), while the NaF-containing devices show an almost negligible *J*–*V* hysteresis (Supplementary Fig. 19b). It is possible that the Na ion can penetrate the perovskite film under an external bias because of its small size[34] (about 0.102 nm). Mobile ions and their accumulation at interfaces are reported to be responsible for the *J*–*V* hysteresis[41]. When using NaF, however, Na is bonded more closely to F, and is therefore localized mostly. The above analysis emphasizes the uniqueness of fluoride to immobilize the counter ions, as compared to other halides.

To test the generality of these findings, we also consider the use of KF as an additive. We fabricate KF-containing PSCs (CsFAMA-K), using the same procedure as for NaF-containing PSCs (CsFAMA-Na). Supplementary Fig. 20 shows that KF-containing PSCs exhibit almost the same PCE as NaF-containing PSCs. In addition, both KF- and NaF-containing PSCs show negligible hysteresis, indicating that KF is also effective in passivating both anions and cations for efficient and stable PSC devices. The analysis above highlights the fact that fluoride ions are desirable for both chemical and electronic passivation in perovskites, and can be combined with a number of alkali metals.

Conclusions

In summary, we have explored an effective approach for simultaneous passivation of both the cation and anion vacancy defects in perovskite materials via chemical bonding enhancement, to improve the efficiency and stability of PSCs. By adding NaF to the triple-cation perovskite absorber, we obtain a PCE of 21.46% (and a certified efficiency of 21.3%) in planar PSCs, which is among the top efficiencies for this type of solar cells. Without any encapsulation, these solar cells exhibit remarkable long-term stability, retaining 90% of their original PCE after 1,000 h under MPP operation conditions

at continuous illumination. The addition of NaF also results in a superb thermal and environmental stability of materials as well as devices. It is found that NaF is indeed present in the perovskite film and forms hydrogen bonds with organic cations within the perovskite crystals, which effectively retards the diffusion of these cations and their dissociation. Fluoride ions also increase the ionic bonding, thus immobilizing both organic cations and halide anions. Passivating the surfaces and grain boundaries through increased chemical bonding, the fluoride ions effectively block the materials degradation pathway at the corresponding interfaces. The present passivation approach that makes use of the high electronegativity of F is generally applicable for improving the stability of perovskite materials by suppressing the formation of halide anion and organic cation vacancies. These findings provide a new approach to the fabrication of highly efficient and stable PSCs.

Methods

Materials. Materials used in experiments include PbI_2 (99.999%, Sigma-Aldrich), CsI (99.9%, Sigma-Aldrich), NaF (AR 98%, Aladdin Industrial Corporation), spiro-OMeTAD (Lumtec), SnO_2 colloid precursor (Alfa Aesar, tin(IV) oxide, 15% in H_2O colloidal dispersion), *N*,*N*-dimethylformamide (DMF; 99.99%, Sigma-Aldrich), dimethylsulfoxide (DMSO; 99.5%, Sigma-Aldrich), isopropanol (99.99%, Sigma-Aldrich), chlorobenzene (99.9%, Sigma-Aldrich), acetone (AR Beijing Chemical Works), ethanol (AR Beijing Chemical Works), aminomethane (CP Beijing Chemical Works), hydrogen iodide (57%, Aladdin Industrial Corporation) and ITO substrate (Shanghai B-Tree Tech. Consult.).

MAX (MAI, MACl, MABr) and FAI were synthesized using the methods reported previously[42]. The details are as follows: 16 ml methylamine water solution (0.1 mol) was added to a 100 ml three-neck flask immersed in a water/ice bath. A certain amount (0.1 mol) of HX acid was slowly dropped into the bottle with continuous stirring. The mixture was refluxed for 2 h under a N_2 atmosphere. Subsequently, the solution was concentrated to a dry solid by using rotary evaporation at 80 °C. This crude product was re-dissolved into 20 ml ethanol, then 100 µl diethyl ether was slowly dropped along the bottle wall and a white product deposited. This recrystallization was repeated three times, and the obtained precipitate was dried in a vacuum oven for 10 h at 40 °C. The final products were sealed in a N_2-filled glovebox for future use. The synthesis procedure for FAI was similar to MAI, except that HI acid was added into an 8.8 g formamidine acetate (0.10 mol) ethanol solution.

Solar cell device fabrication. The ITO substrate was cleaned with ultrapure water, acetone, ethanol and isopropanol successively. After 45 min of ultraviolet–O_3 treatments, a SnO_2 nanocrystal solution was spin-coated on the substrate at 4,000 r.p.m. for 30 s to form a 50-nm-thick film, which was then annealed at 150 °C for 30 min in air. The reference perovskite film was fabricated by a two-step solution process: the PbI_2 (1.3 M, dissolved in DMF/DMSO (9:1, v/v)) mixed with 5% CsI was spin-coated on ITO/SnO_2 at 2,500 r.p.m. for 30 s and annealed at 70 °C for 1 min in a nitrogen glovebox. After cooling the PbI_2-coated substrate to room temperature in a nitrogen glovebox, a mixed organic cation solution (MAI 0.12 M; MABr 0.05 M; MACl 0.07 M; FAI 0.23 M, dissolved in isopropanol) was spin-coated at 2,300 r.p.m. for 30 s and then annealed at 150 °C for 15 min in air. Then the HTM solution, in which a spiro-OMeTAD/chlorobenzene (75 mg ml^{-1}) solution was employed with the addition of 35 µl Li-TFSI/acetonitrile (260 mg ml^{-1}), and 30 µl 4-tertbutylpyridine, was deposited by spin-coating at 3,500 r.p.m. for 30 s. The device was finished by thermal evaporation of Au (80 nm) under vacuum. For the NaX-containing perovskite film, we dissolved a certain amount of NaX with DMF/DMSO (9:1, v/v), and used it as a solvent to dissolve the PbI_2 powder. The optimal content for NaF was about 0.1% mol relative to PbI_2 (Supplementary Fig. 21), and we assumed that all NaF added was successfully incorporated in the final perovskite films because of its high vaporization enthalpy. The other steps are all the same as for the reference sample. For PSC stability tests, we changed the organic cation solution components (MABr 0.05 M; MACl 0.07 M; FAI 0.35 M, dissolved in isopropanol), and the HTM solution was replaced by polymer-modified spiro-MeOTAD to achieve better performance and stability. The other steps are all the same as for the reference and NaF-containing perovskite films.

Material characterization. The morphology of perovskite and PbI_2 thin films and cross-sectional SEM image were measured using a cold field-emission scanning electron microscope (Hitachi S-4800). The X-ray diffraction patterns were collected using a PANalytical X'Pert Pro X-ray powder diffractometer with Cu Kα radiation ($\lambda = 1.54050$ Å). PL was measured by the FLS980 (Edinburgh Instruments Ltd) with an excitation at 470 nm. The ultraviolet–visible absorption spectra were obtained using an UV–visible diffuse reflectance spectrophotometer (UV–vis DRS, Japan Hitachi UH4150). UPS measurements were carried out on an XPS AXIS Ultra DLD (Kratos Analytical). The transient photovoltage and transient photocurrent measurements were performed on a Molex 180081-4320 simulating one-sun working conditions, and the carriers were excited by a 532 nm pulse laser. The electrochemical impedance spectroscopy measurements were determined on an electrochemical workstation (Zahner Company), employing light-emitting diodes (LEDs) driven by Export (Zahner Company). The thermal admittance spectroscopy analyses were conducted on a Zahner Zennium pro Electrochemical Workstation at various temperatures ($T = 210$–350 K) in the dark from 10^0 to 10^6 Hz. A small a.c. voltage of 50 mV was used, and the d.c. bias was kept at zero to avoid the influence of the ferroelectric effect for perovskite material during measurement. For temperature-dependent characterization, the sample was mounted in Cryo Industries Liquid Nitrogen Dewars with a Lake Shore model 335 cryogenic temperature controller. The current density–voltage characteristics of the perovskite devices were obtained using a Keithley 2400 source-measure unit under AM1.5G illumination at 1,000 W m^{-2} with a Newport Thermal Oriel 91192 1,000 W solar simulator. The shading mask and one of our best devices were sent to the National Institute of Metrology, China for certification. The active area was defined as 0.09408 cm^2. External quantum efficiencies were measured by an Enli Technology EQE measurement system. Scanning Kelvin probe force microscopy was performed on perovskite samples in ambient conditions using an MFP 3D-Classic Scanning Probe Microscope (Asylum Research, Inc.). This technique relies on an a.c. bias applied to the tip to produce an electric force on the cantilever that is proportional to the potential difference between the tip and the sample. The scanning was carried out in a dual-pass scan mode; during the first scan the spatial variations in the surface potential were directly measured, and the second scang gives the workfunction by nulling the local electrostatic force gradient arising from the contact potential differences between the AFM tip and the sample surface. The conductive AFM probe was ASYELEC-01-R2 with a Ti/Ir coating and a resonant frequency of 75 kHz. The PLQE data were obtained from a three-step technique through the combination of a 445 nm continuous wave laser, a spectrometer, an optical fibre and an integrating sphere.

Computational methods. Since FA as a cation and I as an anion are the most abundant species in the experimentally studied $(Cs_{0.05}FA_{0.54}MA_{0.41})Pb(I_{0.98}Br_{0.02})_3$ system, the incorporation of Na and F ions at different locations on the surfaces and bulk was investigated using $FAPbI_3$ as a model system. The DFT-optimized lattice parameter of cubic $FAPbI_3$ is 6.360 Å. The surfaces were modelled using slab models consisting of (2 × 2) cells in the *x* and *y* direction and 5 repeating $FAPbI_3$ units constructed from the bulk structure with a vacuum of 15 Å in the *z* direction. Structural optimizations of all structures were performed using DFT implemented in the Vienna ab initio simulation package[43,44]. The Perdew, Burke and Ernzerhof functional within the generalized gradient approximation was used[45]. The outermost *s*, *p* and *d* (in the case of Pb) electrons were treated as valence electrons, whose interactions with the remaining ions were modelled by pseudopotentials generated within the projector-augmented wave method[46,47]. During the structural optimization, all ions were allowed to relax. An energy cutoff of 500 eV and a *k*-point scheme of 3 × 3 × 1 were used to achieve energy and force convergence of 0.1 meV and 20 meV Å^{-1}, respectively. Information on chemical bonding analysis and formation energies of FA^+ vacancies in the reference, NaI- and NaF-containing perovskites is presented in Supplementary Notes 7 and 8.

Reporting Summary. Further information on research design is available in the Nature Research Reporting Summary linked to this article.

Data availability

The data that support the plots within this paper and other findings of this study are available from the corresponding author upon reasonable request.

Received: 2 August 2018; Accepted: 27 March 2019;
Published online: 13 May 2019

References

1. Kojima, A., Teshima, K., Shirai, Y. & Miyasaka, T. Organometal halide perovskites as visible-light sensitizers for photovoltaic cells. *J. Am. Chem. Soc.* **131**, 6050–6051 (2009).
2. Wehrenfennig, C., Eperon, G. E., Johnston, M. B., Snaith, H. J. & Herz, L. M. High charge carrier mobilities and lifetimes in organolead trihalide perovskites. *Adv. Mater.* **26**, 1584–1589 (2013).
3. Snaith, H. J. Perovskites: the emergence of a new era for low-cost, high-efficiency solar cells. *J. Phys. Chem. Lett.* **4**, 3623–3630 (2013).
4. Kim, H.-S. et al. Lead iodide perovskite sensitized all-solid-state submicron thin film mesoscopic solar cell with efficiency exceeding 9%. *Sci. Rep.* **2**, 591 (2012).
5. Lee, M. M., Teuscher, J., Miyasaka, T., Murakami, T. N. & Snaith, H. J. Efficient hybrid solar cells based on meso-superstructured organometal halide perovskites. *Science* **338**, 643–647 (2012).
6. Zhou, H. et al. Interface engineering of highly efficient perovskite solar cells. *Science* **345**, 542–546 (2014).
7. Yang, W. S. et al. High-performance photovoltaic perovskite layers fabricated through intramolecular exchange. *Science* **348**, 1234–1237 (2015).

8. Yang, W. S. et al. Iodide management in formamidinium-lead-halide–based perovskite layers for efficient solar cells. *Science* **356**, 1376–1379 (2017).
9. Tan, H. et al. Efficient and stable solution-processed planar perovskite solar cells via contact passivation. *Science* **355**, 722–726 (2017).
10. *Best Research-Cell Efficiencies* (NREL, 2018); https://www.nrel.gov/pv/assets/pdfs/pv-efficiency-chart.20181221.pdf
11. Zheng, X. et al. Defect passivation in hybrid perovskite solar cells using quaternary ammonium halide anions and cations. *Nat. Energy* **2**, 17102 (2017).
12. Ball, J. M. & Petrozza, A. Defects in perovskite-halides and their effects in solar cells. *Nat. Energy* **1**, 16149 (2016).
13. Sherkar, T. S. et al. Recombination in perovskite solar cells: significance of grain boundaries, interface traps, and defect ions. *ACS Energy Lett.* **2**, 1214–1222 (2017).
14. Kim, J., Lee, S.-H., Lee, J. H. & Hong, K.-H. The role of intrinsic defects in methylammonium lead iodide perovskite. *J. Phys. Chem. Lett.* **5**, 1312–1317 (2014).
15. Duan, H.-S. et al. The identification and characterization of defect states in hybrid organic-inorganic perovskite photovoltaics. *Phys. Chem. Chem. Phys.* **17**, 112–116 (2015).
16. Eames, C. et al. Ionic transport in hybrid lead iodide perovskite solar cells. *Nat. Commun.* **6**, 7497 (2015).
17. Azpiroz, J. M., Mosconi, E., Bisquert, J. & Angelis, F. D. Defect migration in methylammonium lead iodide and its role in perovskite solar cell operation. *Energy Environ. Sci.* **8**, 2118–2127 (2015).
18. Meggiolaro, D. et al. Iodine chemistry determines the defect tolerance of lead-halide perovskites. *Energy Environ. Sci.* **11**, 702–713 (2018).
19. Yin, W.-J., Shi, T. & Yan, Y. Unique properties of halide perovskites as possible origins of the superior solar cell performance. *Adv. Mater.* **26**, 4653–4658 (2014).
20. Du, M. H. Efficient carrier transport in halide perovskites: theoretical perspectives. *J. Mater. Chem. A* **2**, 9091–9098 (2014).
21. Yu, H., Lu, H., Xie, F., Zhou, S. & Zhao, N. Native defect-induced hysteresis behavior in organolead iodide perovskite solar cells. *Adv. Funct. Mater.* **26**, 1411–1419 (2016).
22. Xiao, Z. et al. Giant switchable photovoltaic effect in organometal trihalide perovskite devices. *Nat. Mater.* **14**, 193–198 (2015).
23. Wetzelaer, G.-J. A. H. et al. Trap-assisted non-radiative recombination in organic–inorganic perovskite solar cells. *Adv. Mater.* **27**, 1837–1841 (2015).
24. Berhe, T. A. et al. Organometal halide perovskite solar cells: degradation and stability. *Energy Environ. Sci.* **9**, 323–356 (2016).
25. Aristidou, N. et al. Fast oxygen diffusion and iodide defects mediate oxygen-induced degradation of perovskite solar cells. *Nat. Commun.* **8**, 15218 (2017).
26. Saidaminov, M. I. et al. Suppression of atomic vacancies via incorporation of isovalent small ions to increase the stability of halide perovskite solar cells in ambient air. *Nat. Energy* **3**, 648–654 (2018).
27. Wang, S., Jiang, Y., Juarez-Perez, E. J., Ono, L. K. & Qi, Y. Accelerated degradation of methylammonium lead iodide perovskites induced by exposure to iodine vapour. *Nat. Energy* **2**, 16195 (2016).
28. Juarez-Perez, E. J., Hawash, Z., Raga, S. R., Ono, L. K. & Qi, Y. Thermal degradation of $CH_3NH_3PbI_3$ perovskite into NH_3 and CH_3I gases observed by coupled thermogravimetry–mass spectrometry analysis. *Energy Environ. Sci.* **9**, 3406–3410 (2016).
29. Yang, M. et al. Facile fabrication of large-grain $CH_3NH_3PbI_{3-x}Br_x$ films for high-efficiency solar cells via CH_3NH_3Br-selective Ostwald ripening. *Nat. Commun.* **7**, 12305 (2016).
30. Wang, F. et al. Phenylalkylamine passivation of organolead halide perovskites enabling high-efficiency and air-stable photovoltaic cells. *Adv. Mater.* **28**, 9986–9992 (2016).
31. Marco, N. D. et al. Guanidinium: a route to enhanced carrier lifetime and open-circuit voltage in hybrid perovskite solar cells. *Nano Lett.* **16**, 1009–1016 (2016).
32. Noel, N. K. et al. Enhanced photoluminescence and solar cell performance via Lewis base passivation of organic–inorganic lead halide perovskites. *ACS Nano* **8**, 9815–9821 (2014).
33. Abdi-Jalebi, M. et al. Maximizing and stabilizing luminescence from halide perovskites with potassium passivation. *Nature* **555**, 497–501 (2018).
34. Son, D.-Y. et al. Universal approach toward hysteresis-free perovskite solar cell via defect engineering. *J. Am. Chem. Soc.* **140**, 1358–1364 (2018).
35. Cao, J., Tao, S. X., Bobbert, P. A., Wong, C.-P. & Zhao, N. Interstitial occupancy by extrinsic alkali cations in perovskites and its impact on ion migration. *Adv. Mater.* **30**, 1707350 (2018).
36. Yang, D., Yang, Y. & Liu, Y. A theoretical study on the red- and blue-shift hydrogen bonds of *cis-trans* formic acid dimer in excited states. *Cent. Eur. J. Chem* **11**, 171–179 (2013).
37. Philippe, B. et al. Chemical and electronic structure characterization of lead halide perovskites and stability behavior under different exposures—a photoelectron spectroscopy investigation. *Chem. Mater.* **27**, 1720–1731 (2015).
38. Chen, Q. et al. Controllable self-induced passivation of hybrid lead iodide perovskites toward high performance solar cells. *Nano Lett.* **14**, 4158–4163 (2014).
39. Chen, Q. et al. The optoelectronic role of chlorine in $CH_3NH_3PbI_3(Cl)$-based perovskite solar cells. *Nat. Commun.* **6**, 7269 (2015).
40. Abdi-Jalebi, M. et al. Impact of monovalent cation halide additives on the structural and optoelectronic properties of $CH_3NH_3PbI_3$ perovskite. *Adv. Energy Mater.* **6**, 1502472 (2016).
41. Snaith, H. J. et al. Anomalous hysteresis in perovskite solar cells. *J. Phys. Chem. Lett.* **5**, 1511–1515 (2014).
42. Wang, L. et al. A-site cation effect on growth thermodynamics and photoconductive properties in ultrapure lead iodine perovskite monocrystalline wires. *ACS Appl. Mater. Interfaces* **9**, 25985–25994 (2017).
43. Kresse, G. & Furthmüller, J. Efficiency of ab-initio total energy calculations for metals and semiconductors using a plane-wave basis set. *Comput. Mater. Sci.* **6**, 15–50 (1996).
44. Kresse, G. & Furthmüller, J. Efficient iterative schemes for ab initio total-energy calculations using a plane-wave basis set. *Phys. Rev. B* **54**, 11169–11186 (1996).
45. Perdew, J. P., Burke, K. & Ernzerhof, M. Generalized gradient approximation made simple. *Phys. Rev. Lett.* **77**, 3865–3868 (1996).
46. Blöchl, P. E. Projector augmented-wave method. *Phys. Rev. B* **50**, 17953–17979 (1994).
47. Kresse, G. & Joubert, D. From ultrasoft pseudopotentials to the projector augmented-wave method. *Phys. Rev. B* **59**, 1758–1775 (1999).

Acknowledgements

This work is supported by the National Natural Science Foundation of China (51722201; 51672008; 91733301), National Key Research and Development Program of China grant no. 2017YFA0206701, the Natural Science Foundation of Beijing, China (grant no. 4182026), the Young Talent Thousand Program, National Key Research and Development Program of China grant no. 2016YFB0700700, the National Natural Science Foundation of China (51673025) and Beijing Municipal Science and Technology Project no. Z181100005118002. S.T. acknowledges funding from the Computational Sciences for Energy Research tenure track programme of Shell, NWO and FOM (project no. 15CST04-2). The authors would like to thank W. Zou and J. Wang (Nanjing Tech University) for the PLQE measurement during the revision process, and Z. Dai for providing the dynamic light scattering measurement.

Author contributions

H.Z. and N.L. conceived the idea and designed the experiments. S.T. designed and performed the DFT calculations. Both N.L. and X.N. were involved in all of the experimental parts. Y.C., Z.X., L.W. and H.L. contributed to the fabrication of high-performance PSCs. Z.Q., Y.Z. and L.L. helped to modify the experiments. Y.Lun, X.W. and J.H. performed the KPFM measurements, while Y.Liu, H.X. and Y.G. carried out the UPS and XPS measurement. G.Z. provided the film microstructure analysis. G.B. and C.K.O. assisted in DFT calculations. C.H., Y.B. and S.Y. performed ToF-SIMS measurements. H.Z., Q.C., S.T. and N.L. wrote the manuscript. C.K.O., X.N. and G.B. revised the manuscript. All authors were involved in the discussion of data analysis and commented on the manuscript. N.L. and S.T. have contributed equally to this work.

Competing interests

The authors declare no competing interests.

Additional information

Supplementary information is available for this paper at https://doi.org/10.1038/s41560-019-0382-6.

Reprints and permissions information is available at www.nature.com/reprints.

Correspondence and requests for materials should be addressed to H.Z.

Publisher's note: Springer Nature remains neutral with regard to jurisdictional claims in published maps and institutional affiliations.

Corresponding author(s): Huanping Zhou

Solar Cells Reporting Summary

Nature Research wishes to improve the reproducibility of the work that we publish. This form is intended for publication with all accepted papers reporting the characterization of photovoltaic devices and provides structure for consistency and transparency in reporting. Some list items might not apply to an individual manuscript, but all fields must be completed for clarity.

For further information on Nature Research policies, including our data availability policy, see Authors & Referees.

Experimental design

Please check: are the following details reported in the manuscript?

1. Dimensions			
Area of the tested solar cells	☒ Yes ☐ No	The area of the tested solar cells is 0.09408 cm2 (Methods, Material Characterization)
Method used to determine the device area	☒ Yes ☐ No	The active area was determined by the shading mask which certified by National Institute of Metrology, China (Methods, Material Characterization)
2. Current-voltage characterization		
Current density-voltage (J-V) plots in both forward and backward direction	☒ Yes ☐ No	Figure 4b, Supplementary Figure 12 and Table 1
Voltage scan conditions *For instance: scan direction, speed, dwell times*	☒ Yes ☐ No	JV curves were measured by reverse scan (1.2 V to -0.2 V) and forward scan (-0.2 V to 1.2 V) with a scanning rate of 100 mV/s (voltage step of 10 mV and delay time of 100 ms) (Main text)
Test environment *For instance: characterization temperature, in air or in glove box*	☒ Yes ☐ No	Performance measurements were carried in both nitrogen and air ambient environments (Main text)
Protocol for preconditioning of the device before its characterization	☐ Yes ☒ No	No preconditioning was used
Stability of the J-V characteristic *Verified with time evolution of the maximum power point or with the photocurrent at maximum power point; see ref. 7 for details.*	☒ Yes ☐ No	Maximum power point measurements were conducted (Figure 4c, Figure 5d and Supplementary Figure 18)
3. Hysteresis or any other unusual behaviour		
Description of the unusual behaviour observed during the characterization	☒ Yes ☐ No	The reference cells showed moderate hysteresis while the target cells showed negligible hysteresis (Main text)
Related experimental data	☒ Yes ☐ No	Figure 4b, Table 1
4. Efficiency		
External quantum efficiency (EQE) or incident photons to current efficiency (IPCE)	☒ Yes ☐ No	Supplementary Figure 13
A comparison between the integrated response under the standard reference spectrum and the response measure under the simulator	☒ Yes ☐ No	The integrated Jsc from EQE spectra is consistent with the Jsc from JV measurements (Figure 4b and Supplementary Figure 13)
For tandem solar cells, the bias illumination and bias voltage used for each subcell	☐ Yes ☒ No	No tandem cells reported in this manuscript
5. Calibration		
Light source and reference cell or sensor used for the characterization	☒ Yes ☐ No	Newport Thermal Oriel 91192 1000 W solar simulator is used for the measurements (Methods, Material Characterization)
Confirmation that the reference cell was calibrated and certified	☒ Yes ☐ No	The light intensity was calibrated by reference solar cell by Newport

reference cell and the devices under test

☐ Yes ☐ No

6. Mask/aperture

Size of the mask/aperture used during testing

☒ Yes ☐ No

0.09408 cm2 (Methods, Material Characterization)

Variation of the measured short-circuit current density with the mask/aperture area

☐ Yes ☒ No

We haven't measure the cells with apertures of different sizes

7. Performance certification

Identity of the independent certification laboratory that confirmed the photovoltaic performance

☒ Yes ☐ No

Certified by the National Institute of Metrology, China (NIM, China)

A copy of any certificate(s)
Provide in Supplementary Information

☒ Yes ☐ No

Supplementary Figure 12

8. Statistics

Number of solar cells tested

☒ Yes ☐ No

At least 30 devices for each composition were tested (Supplementary Figure 11)

Statistical analysis of the device performance

☒ Yes ☐ No

Supplementary Figure 11

9. Long-term stability analysis

Type of analysis, bias conditions and environmental conditions
For instance: illumination type, temperature, atmosphere humidity, encapsulation method, preconditioning temperature

☒ Yes ☐ No

Long-term stability including illumination stability, thermal stability, humidity stability and MPP (detailed conditions are shown in main text)

Nature Research, brought to you courtesy of Springer Nature Limited (“Nature Research”)

Terms and Conditions

Nature Research supports a reasonable amount of sharing of content by authors, subscribers and authorised or authenticated users (“Users”), for small-scale personal, non-commercial use provided that you respect and maintain all copyright, trade and service marks and other proprietary notices. By accessing, viewing or using the nature content you agree to these terms of use (“Terms”). For these purposes, Nature Research considers academic use (by researchers and students) to be non-commercial.

These Terms are supplementary and will apply in addition to any applicable website terms and conditions, a relevant site licence or a personal subscription. These Terms will prevail over any conflict or ambiguity with regards to the terms, a site licence or a personal subscription (to the extent of the conflict or ambiguity only). By sharing, or receiving the content from a shared source, Users agree to be bound by these Terms.

We collect and use personal data to provide access to the nature content. ResearchGate may also use these personal data internally within ResearchGate and share it with Nature Research, in an anonymised way, for purposes of tracking, analysis and reporting. Nature Research will not otherwise disclose your personal data unless we have your permission as detailed in the Privacy Policy.

Users and the recipients of the nature content may not:

1. use the nature content for the purpose of providing other users with access to content on a regular or large scale basis or as a means to circumvent access control;
2. use the nature content where to do so would be considered a criminal or statutory offence in any jurisdiction, or gives rise to civil liability, or is otherwise unlawful;
3. falsely or misleadingly imply or suggest endorsement, approval , sponsorship, or association unless explicitly agreed to by either Nature Research or ResearchGate in writing;
4. use bots or other automated methods to access the nature content or redirect messages; or
5. override any security feature or exclusionary protocol.

These terms of use are reviewed regularly and may be amended at any time. We are not obligated to publish any information or content and may remove it or features or functionality at our sole discretion, at any time with or without notice. We may revoke this licence to you at any time and remove access to any copies of the shared content which have been saved.

Sharing of the nature content may not be done in order to create substitute for our own products or services or a systematic database of our content. Furthermore, we do not allow the creation of a product or service that creates revenue, royalties, rent or income from our content or its inclusion as part of a paid for service or for other commercial gain. Nature content cannot be used for inter-library loans and librarians may not upload nature content on a large scale into their, or any other, institutional repository.

To the fullest extent permitted by law Nature Research makes no warranties, representations or guarantees to Users, either express or implied with respect to the nature content and all parties disclaim and waive any implied warranties or warranties imposed by law, including merchantability or fitness for any particular purpose.

Please note that these rights do not automatically extend to content, data or other material published by Nature Research that we license from third parties.

If you intend to distribute our content to a wider audience on a regular basis or in any other manner not expressly permitted by these Terms please contact us at

onlineservice@springernature.com